Applied Clay Science 234 (2023) 106846

Contents lists available at ScienceDirect

Applied Clay Science

journal homepage: www.elsevier.com/locate/clay

Friction influence on constant volume saturation of bentonite mixed pellet-block samples, a numerical analysis

Liliana Gramegna [a,*], María Victoria Villar [b], Frédéric Collin [c], Jean Talandier [d], Robert Charlier [c]

[a] Politecnico di Milano, Department of Civil and Environmental Engineering, P.zza Leonardo da Vinci 32, 20133 Milano, Italy
[b] Centro de Investigaciones Energéticas, Medioambientales y Tecnológicas (CIEMAT), Avd. Complutense 40, 28040 Madrid, Spain
[c] Université de Liège, Département ArGEnCo - Géotechnique, Géomécanique et Géologie de l'Ingénieur - 4000, Liège 1, Belgium
[d] ANDRA - Agence Nationale pour la gestion des Déchets Radioactifs, 92298 Châtenay-Malabry, France

ARTICLE INFO

Keywords:
Bentonite
Numerical simulation
Friction analysis
Experimental procedures
Isochoric test

ABSTRACT

Bentonite-based materials are employed in some nuclear waste disposal concept designs to seal underground tunnels and shafts. In some cases, these barriers consist of two parts: highly compacted blocks and granular buffer material consisting of pellets. These two components have highly distinct initial properties in terms of dry density, water content, and microstructure, but, at full water saturation, those tend to homogenise. However, the simultaneous application of pellets and blocks in the same barrier section creates challenges for understanding and modelling system performance that must be tackled. Therefore, this work merges experimental and computational approaches to better understand the hydro-mechanical processes that take place throughout the interaction of the various assemblies with one another and with the environment during hydration.

Hence, the role of a variety of material configurations, considering simultaneously compacted blocks and pellets, and hydration boundary conditions is analysed giving great insight about intermediate saturation states. Discrepancies between experimental measurements and model results were explained by the effect of friction after a sensitivity analysis performed with the finite element code LAGAMINE. Results from experiments and calculations were in good agreement and offer supplementary knowledge about a relevant amount of the numerous phenomena (for instance related to dry density evolution and water distribution inside the sample) taking place during initial heterogeneous bentonite samples resaturation in isochoric conditions.

1. Introduction

Bentonite-based materials are chosen as the main component of engineered barriers in the context of nuclear waste geological disposal due to their large swelling capacity upon hydration, very low permeability in saturated conditions, and radionuclide retention capacities (Cui, 2017; Pusch, 1979; Sellin and Leupin, 2014). Bentonite-based materials are considered to seal underground galleries and shafts, as in the French CIGEO concept (Labalette et al., 2009), yet, as employed in the EB experiment, those may also be placed in direct contact with canisters containing nuclear waste (Alonso et al., 2010). The latter one, in particular, is a good example of how compacted bentonite blocks and bentonite granular material can be used together. Although, most experimental research and constitutive models in the past have mostly focused on bentonite compacted blocks (in the following denoted CB) (Wang et al., 2013, Dixon et al. 2002, Mayor et al. 2005 among many), investigations on high density bentonite pellets combined with powdered bentonite are gaining increasing interest (Molinero et al., 2017; Dardé et al., 2018; Liu et al., 2019; Liu et al., 2020a,b; Zhang et al., 2020 Bernachy-Barbe et al., 2020), even though they were already proposed decades ago (Van Geet et al., 2005; Salo and Kukkola, 1989). Pellets combinations provide obvious benefits in terms of high-volume emplacements and the minimization of technological gaps in underground shafts. This is due to the adoption of pneumatic stowing techniques, which enable backfilling with a simpler and potentially robotized procedure, which is particularly relevant in the case of high-level radioactive waste (Alonso et al., 2010). The pore structure distribution of such pellet combinations (due to the inherent nature of the assembly and this emplacement approach) can have an impact on the mechanical and hydraulic properties (Navarro et al., 2020). This pore structure distribution is made up of micro-pores (i.e. from high dry density pellets) and macro-pores (i.e. from the low dry density crushed

* Corresponding author.
E-mail address: liliana.gramegna@polimi.it (L. Gramegna).

https://doi.org/10.1016/j.clay.2023.106846
Received 11 November 2022; Received in revised form 17 January 2023; Accepted 27 January 2023
Available online 6 February 2023

pellets component).

The hydro-mechanical investigation of bentonite multi-structure assemblies during hydration is a difficult task. The goal of this article was to integrate experimental and numerical procedures in order to better understand the hydro-mechanical phenomena that occur during the interaction of the various assemblies between each other and with the experimental equipment when they are hydrated. Most of these interactions have an impact on the formation and evolution of experimental and numerical observations, but they have never been thoroughly studied.

CIEMAT's large-scale oedometer tests (MGR) were analysed for this purpose. This experimental study, reported in Villar et al. (2021) considered a variety of material configurations and hydration boundary conditions, and provided great insight about intermediate saturation states.

In this paper, the MGR experimental tests are briefly explained and then numerically modelled. From both a hydraulic and a mechanical perspective, correlations between experimental and numerical results focused on intermediate saturation phases of the bentonite-based materials.

Even though the analysed materials' heterogeneous initial pore structure distributions are well-known, the numerical technique represented the layers in the framework of continuum mechanics. The Barcelona Basic Model (Alonso et al., 1990) for bentonite mechanical behaviour was preferred over other more advanced but complex available models owing to its great simplicity, robustness and efficiency. On the other hand, micro and macro pores features and influence is modelled in with a double porosity model for the water retention behaviour and water permeability evolution (Dieudonné et al., 2017).

By integrating results of experimental data at dismantling and numerical simulations, this work allowed assessing the validity of the proposed numerical model predictions.

In addition, the development of friction between the material samples and the cell wall was identified as major responsible for unexpectedly lower pressure measurements by numerous authors (Molinero et al. (2018), Talandier (2018), Baryla et al. (2018)), it was evaluated in this work. Indeed, it was investigated thanks to the introduction of an interface element (similarly to Abed and Solowski, 2019 and Talandier, 2018).

2. Materials and experimental method

The goal of this set of tests was to examine the saturation in isochoric conditions of a selection of FEBEX bentonite samples made up of one layer of pellets and one layer of compacted material with different initial dry densities and pore-structure distributions (Villar et al., 2021).

The FEBEX bentonite was extracted from the Cortijo de Archidona quarry (Almería, Spain) and is composed in ~90% of a montmorillonite-illite mixed layer, with also variable quantities of quartz, plagioclase, K-felspar, calcite, and cristobalite-trydimite. The main exchangeable cations are calcium, magnesium and sodium (ENRESA, 2006; Villar, 2017). A detailed hydro-mechanical characterisation of the pellets mixture was performed by Hoffmann (2005).

The experimental device consisted of a large-scale stainless steel oedometer cell with interior diameter of 100 mm and a sample length of 100 mm. It is discussed in more detail in Villar et al. (2021). Deionized water was injected through the bottom surface with a very small hydraulic head of about 140 cm, while water intake was recorded continuously. The top side of the sample was open to laboratory conditions to guarantee trapped air evacuation. The pellet layer (PL in the following) made up the bottom part of the samples in direct contact with the water source (tests MGR21, 23, 24, and 25), whereas test MGR27 had an inverted configuration (i.e. bottom layer composed of compacted bentonite block). So, hydration proceeded through CB or through pellets.

Five different tests were considered in this paper: tests MGR23 and MGR 27 stopped after more or less full saturation; tests MGR21, 23, 24, and 25 at the 34th, 210th, 14th, and 76th day after the beginning of hydration. Upon dismantling the dry density and water content of the bentonite, as well as the pore size distribution by mercury intrusion porosimetry, were determined at different positions along the length of the sample (Villar et al., 2021). This provided additional information about the evolution of dry density and water content during hydration. Further experimental samples specifications can be found in Fig. 1 and Table 1.

Given similar initial states and hydration boundary conditions, the final states of tests MGR21, 24 and 25 were assumed to be intermediate states of test MGR23.

3. Geometric configuration, constitutive modelling and material parameters

The numerical simulations were done with the finite element code Lagamine (Collin et al., 2002) with the hydro-mechanical constitutive models employed in Gramegna (2020, 2022).

The numerical bentonite samples consisted of 800 eight-noded isoparametric elements representing the bentonite materials (400 for the pellets and 400 for the CB). The problem was assumed to be axisymmetric and subjected to oedometer conditions (Fig. 1).

The pellet and CB-layers materials presented the same dry density in all the numerical simulations, but the water content of the PL fluctuated between the experimental tests, and was the same for the block components in all the cases (Table 1). The pellets-mixture significant heterogeneity was well-known, but in the current modelling approach, the PL, as well as the CB-layer, was considered homogeneous, with the same hydro-mechanical characteristics and state throughout the domain. Same hydro-mechanical properties and hydro-mechanical state were set with initial uniform suction s related to the degree of saturation S_r, (obtained thanks to the corresponding water content w and dry density ρ_d) via the adopted dry density dependent water retention model. The numerical model's initial water contents w were comparable to those found empirically at the initial condition.

The samples were hydrated from the bottom face (red line, Fig. 1) assuming a 1000-s interval for the suction decrease from the initial value to the experimental boundary conditions.

3.1. Mechanical behaviour

The interrelated and simultaneous multi-physical and multi-scale phenomena that occur during bentonite hydration are characterised for their complexity and were reproduced via the Barcelona Basic Model (BBM) (Alonso et al., 1990).

The model was formulated adopting as stress variables net stress $\boldsymbol{\sigma}$ and suction s:

$$\boldsymbol{\sigma} = \boldsymbol{\sigma}_T - u_a \boldsymbol{I} \tag{1}$$

With $\boldsymbol{\sigma_T}$ the total stress tensor, u_a the air pressure for $s > 0$ and $\boldsymbol{I}$ the identity tensor.

With respect to isotropic stress conditions, the elastic strain evolution was associated to mean net stress p and suction s (Eq. (2)) via elastic compressibility coefficients for change in stress (κ) and in suction (κ_s):

$$d\varepsilon_v^e = \frac{\kappa}{1+e}\frac{dp}{p} + \frac{\kappa_s}{1+e}\frac{ds}{s+u_{atm}} \tag{2}$$

Stress dependence of the swelling strain for change in suction was also considered (Eq. (3)):

$$\kappa_s(p) = \kappa_{s0} * exp\left(-\alpha_p * p\right) \tag{3}$$

The evolution of the preconsolidation pressure $p_0(s)$ was described according to the concept of increasing the elastic domain with increasing suction (Eq. (4)) as well as the rate of increase of the plastic

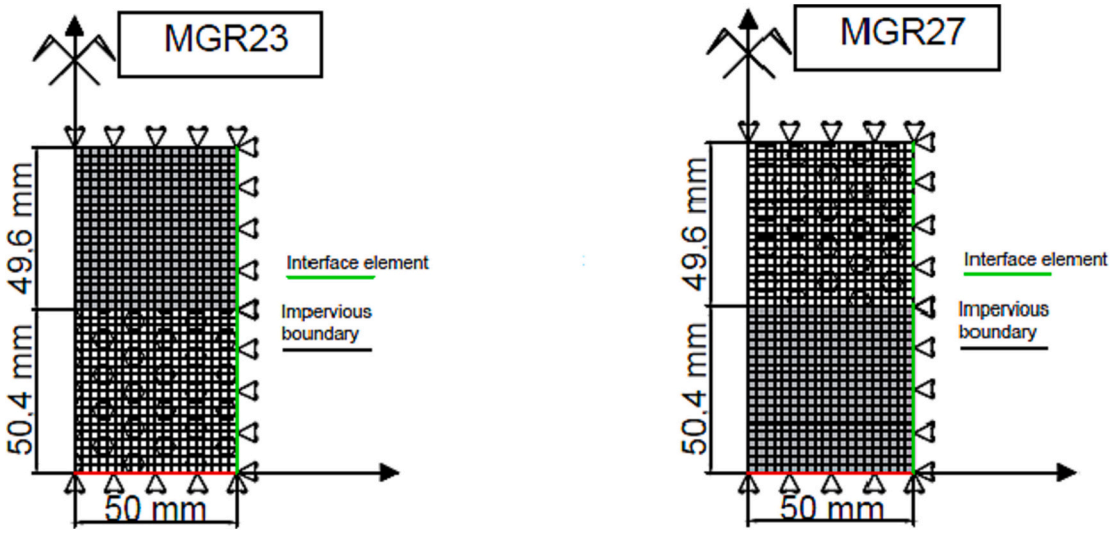

Fig. 1. Characteristics of the considered samples and boundary conditions of the model.

Table 1
Initial state and characteristics of the experimental samples and numerical simulations.

Tests	MGR21		MGR23		MGR24		MGR25		MGR27	
	Exp	Num	Exp	Num	Exp	Num	Exp	Num	Exp	Num
Position of the PL	Bottom		Bottom		Bottom		Bottom		Top	
Pellet height [mm]	49.7	49.6	50.0	49.6	50.2	49.6	49.9	49.6	50.0	50.4
Pellet dry density [Mg/m^3]	1.26	1.28	1.30	1.28	1.28	1.28	1.30	1.28	1.30	1.28
Pellet water content [%]	9.50	9.80	3.5	4.90	5.7	4.90	3.17	4.90	3.5	4.90
Position of the CB-layer	Top		Top		Top		Top		Bottom	
Block height [mm]	50.1	50.4	49.8	50.4	49.7	50.4	50	50.4	49.8	49.6
Block dry density [Mg/m^3]	1.60	1.60	1.60	1.60	1.62	1.60	1.59	1.60	1.60	1.60
Block water content [%]	13.3	13.6	14.2	13.6	13.7	13.6	14.10	13.6	14.2	13.6
Diameter [mm]	100	100	100	100	100	100	100	100	100	100
Total height [mm]	99.8	100	99.8	100	99.9	100	99.9	100	99.8	100
Total dry density [Mg/m^3]	1.43	1.44	1.45	1.44	1.45	1.44	1.44	1.44	1.45	1.44
Total water content [%]	11.6	11.9	9.4	9.76	10.1	9.76	9.18	9.76	9.4	9.76
Test duration [days]	34	34	210	210	14	14	76	76	278	278

compressibility coefficient $\lambda(s)$ with suction (Eq. (5)).

$$p_0(s) = p_c\left(\frac{p_0^*}{p_c}\right)^{\frac{\lambda(0)-\kappa}{\lambda(s)-\kappa}} \quad (4)$$

$$\lambda(s) = \lambda(0)[(1-r)exp(-\omega s)+r] \quad (5)$$

The parameters for the model were derived from swelling consolidation oedometer tests performed by Lloret et al. (2003) on a similar dry density compacted FEBEX bentonite, whereas data from Hoffmann et al. (2007) were adopted for the PL (Table 2).

3.2. Water retention behaviour

The selected water retention model (Dieudonné et al., 2017) was expressed in terms of water ratio e_w, defined as the product of void ratio e and degree of saturation S_r. It was then assumed that the total water content can be decomposed as the sum of two contributions, coming from the water adsorbed in micropores e_{wm} and water stored in macropores e_{wM}. Moreover, the model also accounted for the variation of micro-pores upon saturation via:

$$e_m = e_{m0} + \beta_0 e_w + \beta_1 e_w^2 \quad (6)$$

The distinction between micro- and macro-pores relied on experimental observations and theoretical interpretations provided in Romero et al. (2011) and Della Vecchia et al., (2015). The selected double porosity dry density dependent water retention model did not

Table 2
Parameters of the mechanical model.

Symbol	Unit	Description	CB	Pellets mixture
ρ_d	[Mg/m^3]	Dry density	1.60	1.28
κ	[−]	Elastic compressibility coefficient for changes in mean net stress	0.012	0.074
κ_s	[−]	Elastic compressibility coefficient for changes in suction	0.12	0.075
α_p	[−]	Parameter controlling the stress dependency of the swelling strain for change in suction	4.4×10^{-8}	3×10^{-6}
p_0*	[MPa]	Pre-consolidation pressure for saturated state	1.6	0.65
p_c	[MPa]	Reference pressure controlling the shape of the LC curve	0.395	0.325
$\lambda(0)$	[−]	Slope of the saturated virgin consolidation line	0.12	0.20
r	[−]	Parameter defining the minimum soil compressibility	0.55	0.70
ω	[Pa]	Parameter controlling the soil stiffness	0.25	0.008
φ	[°]	Friction angle	20	26
ν	[−]	Poisson ratio	0.25	0.35
$c(0)$	[MPa]	Cohesion in saturated conditions	0	0
k	[−]	Parameter controlling the increase of cohesion of increase of suction	0.0046	0.0046

distinguish the initial pore structure distributions of the considered assemblies, thus a unique set of parameters corresponding to the calibration proposed by Dieudonné et al. (2017) for Febex bentonite was selected (Table 3).

3.3. Flow properties

The permeability evolution was calculated using an extended Kozeny-Carman model to account for the double structure nature of compacted bentonite-based materials. According to Romero (2013), the macro-void ratio e_M (given here as $e_M = e - e_m$) should replace the total porosity used in the original model. According to Eq. (6), upon water saturation in isochoric conditions, macro porosity decreased, resulting in permeability decrease.

The parameters for the water permeability evolution (Table 4) were calibrated by best fitting the responses of the water intake time evolution of test MGR23. Consequentially, the model was validated by comparing its prediction on the swelling pressure kinetics and final dry density and water content distributions with the experimental results.

3.4. Interface properties

Mechanical displacements, water pressure, and gas pressure can vary on either side of a discontinuity. However, since each side of the interface communicates with each other, their mechanical and hydraulic evolution cannot be treated separately. Indeed, in this work, friction was considered between the material sample and the cell wall (i.e. a purely mechanical interaction), which was simulated via the hydro-mechanical zero-thickness element implemented in LAGAMINE (Cerfontaine et al. 2015).

Forty 3-noded isoparametric interface elements were used to reproduce the interaction between the bentonite materials and the cell wall (green line Fig. 1).

The interface mechanical parameters are presented in Table 5. The choice of the friction angle is discussed further in this work.

4. Results

4.1. Hydration process

The experimental and numerical evolution through time of water intake and top axial pressure for the considered tests is provided in Fig. 2 and Fig. 3.

Water income to reach full saturation was slightly dissimilar during experimental tests (250 ± 12 g), due to small unavoidable differences in initial dry density and water content, which were intrinsic to the materials nature and to samples preparation (Table 1). On the other hand, numerical simulations allowed setting identical features in the layers for all the tests avoiding reality's inevitable dispersion. Tests MGR21, 23, 24 and 25 experimental outcomes were very difficult to distinguish in the first phase of hydration and the water injection curves nearly overlapped and totally coincided in the numerical case. Water intake evolution over time Fig. 2 appeared evidently different between the case of hydration provided from the PL (tests MRG21, 23, 24 and 25) and the one taking place through the CB part (tests MGR27), both from experimental and numerical points of view. In the tests in which hydration was provided from the PL, water intake was quicker with respect to the case in which saturation took place from the CB part. This occurrence was certainly related to the different permeability between the initial low-density PL and the initial high-density CB-layer.

Swelling pressures were measured axially on the top end of the samples. Experimental and numerical results showed similar characteristics. Top axial swelling pressure experimental results of the first four tests Fig. 3 showed similar pressure evolutions with time, both experimentally and numerically. An initial quick swelling pressure increase characterised all the tests, particularly evident in tests MGR21, 23, 24 and 25 due to the larger top axial pressure magnitude. Indeed, these first pressure peaks were reached after 30–40 days for test MGR23 and 25. A second phase, which consisted in an intermediate phase of a small pressure decrease, was observed only in tests MGR23 and 25, since tests MGR21 and MGR24 were stopped far earlier. The last phenomenon, occurring for high level of saturation ($S_r > 95\%$), eventually included a new increase of the swelling pressure until a final stabilisation. The experimental top final axial swelling pressure value for test MGR23 was equal to 3 MPa. On the other hand, for test MGR27, the recorded behaviour appeared quite different. The first pressure increase reached a lower pressure value equal to 1 MPa and it was not followed by the above-mentioned pressure decrease. The recorded top axial swelling pressure was almost constant, very slowly increasing until the 200th day of the test time. It finally presented an almost imperceptible last increase of swelling pressure (much later with respect to MGR23) and a pressure stabilisation at 1.5 MPa (half of the final values of test MGR23).

Numerical simulations compared quite well with the experimental results with respect to top axial pressure. As an example, the comparisons between experimental results and numerical simulations with respect to top axial swelling pressure over time for tests MGR23 and MGR27 are showed Fig. 4. The numerical results concerning swelling pressure time evolution at the bottom face of the samples and radial at the cell wall at z = 25 mm and z = 75 mm from the wetting surface are additionally reported in Fig. 4. Those were not measured during the

Table 3
Parameters of the water retention curve model.

Symbol	Unit	Description	CB	Pellets mixtures
ρ_d	[Mg/m^3]	Dry density	1.60	1.28
e_{m0}	[−]	Microstructural void ratio for the dry material	0.35	
β_0	[−]	Parameters quantifying the swelling	0.15	
β_1	[−]	potential of the aggregates	0.35	
C_{ads}	[MPa^{-1}]	Parameter associated to the desaturation rate of the soil	0.0028	
n_{ads}	[−]	Parameter controlling the WRC curvature in the high suction range	0.78	
n	[−]	Material parameters for macro-pore retention capacity	3	
m	[−]		0.15	
A	[MPa]	Parameter controlling the dependence of the air-entry pressure on the macro-structural void ratio	0.24	

Table 4
Parameters of the permeability evolution model.

Symbol	Unit	Description	CB	Pellets mixtures
C_k	[m^2]	Reference permeability	2.8 ×10^{-20}	2.8 ×10^{-20}
expm	[−]	Model parameters	1.2	0.9
expn	[−]		0.1	0.1
γ	[−]	Parameter controlling the evolution of relative permeability	3.4	3

Table 5
Interface mechanical properties.

Symbol	Unit	Description	
K_t	[N/m^3]	Penalty coefficient in the normal direction	10^{11}
K_l	[N/m^3]	Penalty coefficient in the longitudinal direction	10^{11}
φ	[°]	Friction angle	7
μ	[−]	Friction coefficient	0.125
c'	[MPa]	Cohesion	0

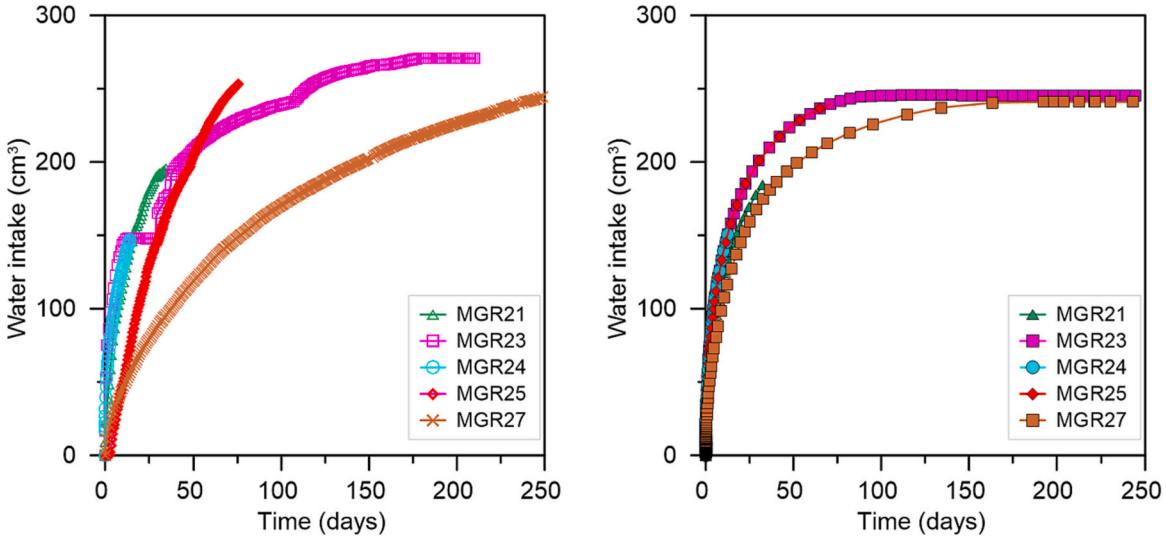

Fig. 2. Water intake evolution over time: experimental and numerical results.

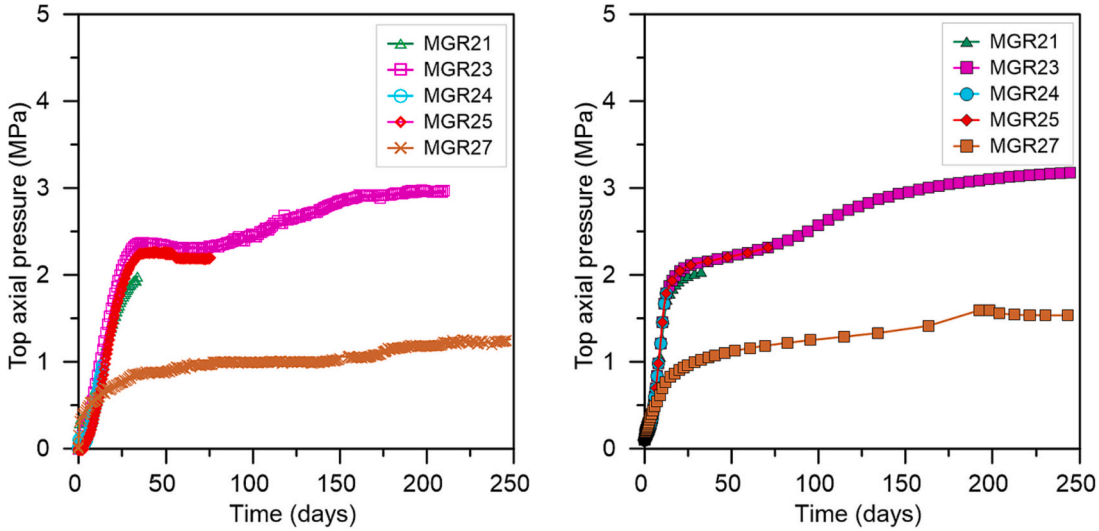

Fig. 3. Top axial pressure evolution over time: experimental and numerical results.

experimental campaign. The trend of the transient phase was well reproduced as well as the stabilisation time. The top axial swelling pressure of the numerical simulations for tests MGR23 and 27 compared impressively fine with the experimental results since the very beginning of hydration until the final stabilised value. The numerical top axial and bottom swelling pressures of all the tests reasonably differed due to the friction phenomena modelled at the contact with the cell wall. Friction developed since the very beginning of the hydration phase. The difference between the top and bottom pressure measurements increased up to a maximum value of approximately ~1 MPa. Subsequently it remained constant. At this moment, the resistance to the sliding exerted on the cell wall could not increase any further. Thus, the axial pressure disparity remained constant for all the tests and the sliding of the material sample with respect to the cell wall occurred.

The axial and radial numerical swelling pressure measurements close to the CB-layers did not differ significantly between numerical simulations of tests MGR23 and MGR27, as well as the ones in the PLs. Namely, the numerical axial swelling pressure measured iclose to the CB-layers was typically much higher with respect to the one in the pellets material for the same saturation level. The comparison between the experimental top axial swelling pressure measurement of test MGR23 and the numerical bottom one of test MGR27, both corresponding to CB, appeared of particular interest. The two values did not differ sensitively neither did the experimental top axial swelling pressure measurement of test MGR27 and the numerical bottom one of test MGR23, both corresponding to PL.

4.2. Final physical state

Dry density and water content at different locations from the hydration surface were determined in the laboratory thanks to post-mortem analyses by cutting the overall assemblies in subsamples (Villar et al., 2021). These values, which are inversely related, were compared to the numerical results Fig. 5.

For instance, in test MGR24 the material pellets portion closest to the wetting surface experienced volume increase starting from an initial dry density equal to $\rho_d = 1.30$ Mg/m^3 up to $\rho_d = 1.20$ Mg/m^3, whereas the upper part of the pellet layer was subjected to compaction exerted by the swelling of the bottom part of the pellet layer and the one of the upper CB. Thus, starting from $\rho_d = 1.30$ Mg/m^3, it reached $\rho_d = 1.35$ Mg/m^3. The upper CB showed very low volume increase with a minimum dry density value equal to $\rho_d = 1.55$ Mg/m^3 in the vicinity to the PL.

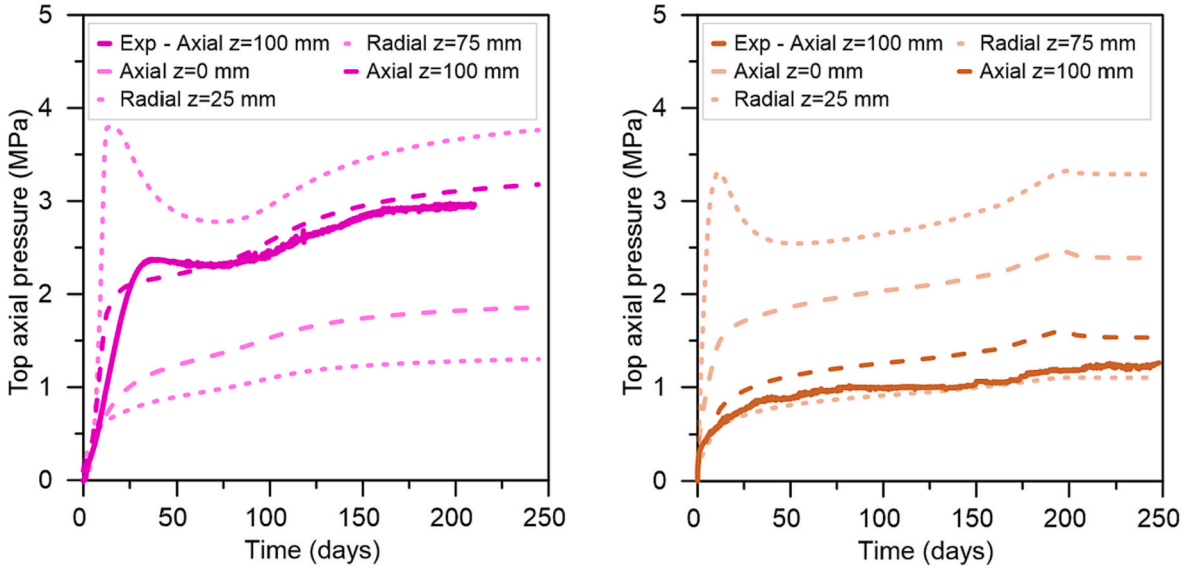

Fig. 4. Total pressure evolution for tests MGR23 (hydration at constant water pressure through PL) and test MGR27 (hydration at constant water pressure through CB-layer). Comparison between experimental results on the top axial measurement of the sample and numerical simulations at the axial top and bottom face of the sample and radial at the cell wall at z = 25 mm and z = 75 mm from the wetting surface.

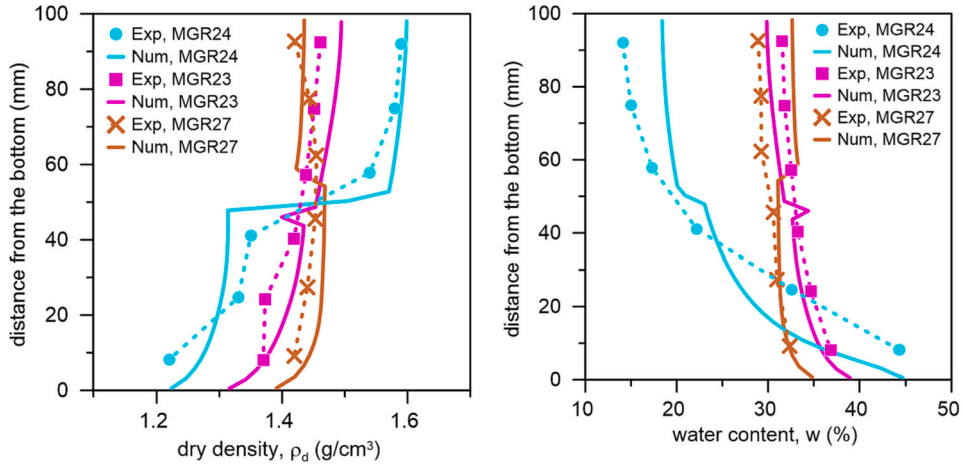

Fig. 5. Final dry density and water content along the samples of tests MGR24, MGR23, and MGR27. Comparison between experimental results and numerical simulation.

Post-mortem analyses of test MGR23 represented the final state of the hydration process corresponding to the full saturation of the sample. The PL revealed a general volume reduction with dry density spanning between $\rho_d = 1.38$ Mg/m^3 in the lowest part and $\rho_d = 1.42$ Mg/m^3 at the boundary with the top CB-layer. Accordingly, the upper CB part indicated a general and uniform volume increase corresponding to a final dry density equal to $\rho_d = 1.45$ Mg/m^3.

Dry density at dismantling of test MGR27 differed noticeably from the other experimental results, with the most homogeneous final water content. The lowest dry density was found on the top and bottom parts of the sample regardless the initial dry density of the corresponding material. The densest part was detected approximately at the central part of the sample. In general, the bottom part of the CB underwent swelling, whereas the top PL experienced compaction. The most compacted part of the sample corresponded indeed to the pellets portion in direct contact with the CB, similarly with the other cases, as well as the most swollen part of the CB, which was the one in direct contact with the hydration front (namely the lower one).

5. Discussion

5.1. General overview on the hydration process and physical state evolution

Experimental and numerical tests MGR23 (21, 24, 25) and MGR27 differed only for the configurations of the two layers, since the hydration boundary conditions and materials initial states were exactly the same. Namely, for test MGR23 the PL was placed on the bottom part of the sample in direct contact with the saturating surface, whereas for test MGR27 the bottom layer in direct contact with the water source was composed of the compacted bentonite block material. In this case, the saturation process slowed down according to the lower permeability of the bentonite CB compared to the one of the PL, related to the much higher dry density and to the intrinsic pores structure nature, tackled by the hydraulic constitutive models. Hence, the MGR27 experimental results and numerical simulation showed that the water intake process was initially slower than the one experimentally and numerically recorded for test MGR23. Afterwards, the injection rates decreased but less than in the MGR23 case. With respect to these experimental conditions, it

appeared that the configuration with the denser material in contact with the water source causes a larger full saturation time, which can be particularly relevant in the case of real scale structure. The water inflow numerical results of test MGR27 did not correspond precisely to the experimental outcomes in terms of kinetics, but those were able to reproduce the above-mentioned trends.

Tests MGR21, MGR23, MGR24 and MGR25 presented significant top axial swelling pressure development only for average saturations higher than $S_r = 60\%$. Concerning test MGR23, a swelling pressure increase was observed at average saturation level equal to $S_r = 70\%$. This pressure increase took place between the 10th and the 28th days of the experimental test time, when 150 cm^3 of water had been injected. The top axial swelling pressure for test MGR27 increased up to 1 MPa for an average saturation level of $S_r = 60\%$. Then it remained almost constant until $S_r = 80\%$ and it increased again until 1.5 MPa when full saturation occurred.

Emphasis should be given to the comparison between tests MGR23 and MGR27. The top axial swelling pressure peak approximately equal to 2.3 MPa for MGR23, which delimitated the elastic domain in the framework of elasto-plasticity (Lloret et al., 2003), was observed for average saturation of $S_r = 76\%$. This average saturation corresponded to water intake quantities equal to ~150 g. The boundary of the elastic domain was very difficult to determine for test MGR27, but a change of slope was observed after 1 MPa of top axial swelling pressure.

Test MGR27 presented a very distinct behaviour with respect to tests MGR21, 23, 24 and 25 despite the same water injection pressure. Top axial pressure developed slightly before and when the degree of saturation was lower than in the other tests (30%). This was related to the fact that the block denser bentonite part, main responsible for the swelling pressure development, was immediately reached by the saturation front. Thus, the pressure development process speeded up. Especially with respect to this, during test MGR21, 23, 24 and 25, the overall water inflow was firstly injected in the PLs, hence, it caused the modification of the pores-structure according to Eq. (6) and the following permeability decrease. Consequentially, the swelling pressure development was marginally delayed with respect to the case in which it occurred in the CB part directly. The very distinct hydration dynamics taking place in tests MGR23 and MGR27 did not influence notably the swelling development of the CB layer. Even thought, for test MGR23 the waterfront had firstly to saturate the PL layer, this latter one presented a high permeability allowing in any case an almost immediate activation of the CB swelling advancement, similar to the one related to the direct saturation of test MGR27.

The axial total stress was not considered uniform on each sample due to the friction development with the cell wall and it explained the large discrepancy between the final top axial swelling pressure values of test MGR23 with test MGR27, considering the same average dry density of the samples. The effect of friction on swelling pressure measurements was already met by a number of authors ((Molinero et al., 2018), (Talandier, 2018), (Baryla et al., 2018)), nevertheless, it was never precisely determined and very few information was available (Dueck et al., 2019; Dueck and Nilsson, 2010). Thus, this numerical analysis helped to provide complementary information with respect to the much more variable and difficult to control experimental tests.

Simultaneously, the dry density distribution of those tests corresponding to constant water pressure hydration strategy and PL at the bottom (namely tests MGR21, 23, 24 and 25), as the saturation began, started to decrease firstly in those material portions located at the bottom part of each layer. More precisely, both in pellets and CB-layers, the parts which swelled the most were the bottom ones. For the pellets, that material was in direct contact with the wetting surface, whereas for the CB, that zone was the one immediately hydrated from the pellets material. With respect to the upper PL part, in direct contact with the swelling compacted bentonite block, compaction was observed. The upper part of the CB-layer was the one that swelled the last. As a result, a certain dry density gradient in the hydration direction was established. While the saturation process continued, with the concomitant swelling of the upper block and compaction of the bottom PL, the dry density gradient almost disappeared. It was possible to observe that the numerical results compared remarkably well the experimental dry density distributions for all the tests, corresponding to different average saturations (Fig. 5).

Test MGR27 dry density evolution was characterised by an immediate development of dry density gradient differently from tests MGR21, 23, 24 and 25. The CB portion in direct contact with the wetting surface immediately swelled. This swelling did not cause the compaction of the top CB part but its sliding. Once again, the PL was the most compacted by the CB sliding given the lower swelling capacity related to the lower initial dry density. As the saturation front proceeded from the bottom, all the bentonite CB experienced a general and quite uniform volume increase. The concomitant volume reduction in the top PL appeared uniform in the central part, but with a small dry density layer at the contact with the cell wall due to friction. In correspondence with experimental results, the numerical final saturated state of test MGR27 presented the lowest dry density in the top and bottom part of the sample, with a general compaction of the central part.

As observed for the experimental results, the numerical water content distributions and evolutions followed trends related to the dry density, as a result of the strongly coupled hydro-mechanical phenomena taking place during bentonite hydration.

5.2. Sensitivity analysis on the influence of friction coefficient

The influence of frictional phenomena development between bentonite materials and laboratory equipment on swelling capacity measurements during hydration are not fully understood yet. According to the very complex experimental characterisation, holding highly coupled hydro-mechanical mechanisms, very few experimental data are available and pioneering numerical work was attributed to Abed and Solowski (2019), Baryla et al. (2018) and Stavropoulou (2017).

In general friction phenomena were modelled via the Coulomb criteria, in which the resistance to sliding is given by a friction coefficient ($\mu = tg\phi$) multiplying the normal pressure exerted on a surface (possibly summed up with the cohesion) (Eq. (7)). Namely, this coefficient, proportional to the radial stress exerted on the cell wall, controls the maximum exerted tangential stress value before sliding.

$$\tau \leq p_N tan\phi + c \tag{7}$$

Thus, radial pressure at several location and top and bottom axial pressure measurements are needed in order to determine experimentally the friction coefficient in oedometer conditions. Nevertheless, in the considered experimental campaign, only the top axial swelling pressure was recorded.

For this reason, a numerical sensitivity analysis was performed in order to determine the influence of the friction coefficient between the bentonite material and the cell wall on experimental and numerical responses neglecting the role of radial stress.

For this purpose, tests MGR23 and 27 were considered. Those tests presented exactly the same initial conditions and characteristics, but final swelling pressure values respectively equal to 3 MPa and 1.5 MPa.

Hence, the following analysis on friction phenomena aimed to justify the experimental results and to propose a complementary numerical procedure to determine the friction coefficient.

Four cases were analysed: a model without friction in which the material was free to slide with respect to the cell wall (i.e. $\mu = 0$); a model in which sticking contact was modelled and the material was glued to the cell wall (i.e. $\mu = \infty$); two intermediate arbitrary values in between the limit cases $\mu = 0.360$ and $\mu = 0.180$ (respectively $\phi = 19.8^\circ \approx 20^\circ$ and $\phi = 10.2^\circ \approx 10^\circ$) in which the material could slide with respect to the cell wall only if the failure criteria was met to analyse the effect of such parameter. The friction coefficient was considered constant on the entire cell wall surface regardless the material with which it is in contact (i.e. CB or pellets).

The comparison between numerical results considering different friction coefficients with the cell wall with respect to the total axial pressure on the top and bottom faces over time is given in Fig. 6. For the case $\mu = 0$, in which friction between material and the cell wall was not considered, the axial top and bottom swelling pressure measurements overlapped for both tests MGR23 and MGR27, reaching final stabilised swelling pressure values equal approximately to 2 MPa in both cases.

On the other hand, when sticking contact was assumed between the material and the cell wall, the top and bottom axial swelling pressure measurements differed noticeably. In general, the measurements recorded in the CB sides presented much higher values with respect to the measurements of the PL sides. For test MGR23, the axial pressure stabilised value was equal to 4 MPa in top CB-layer and 1.20 MPa in the bottom pellets one, with ~3 MPa of discrepancy. In test MGR27, the axial pressure stabilised value in the bottom CB-layer was equal to 3 MPa and 1 MPa in the top pellets layer, with 2 MPa final difference.

In the intermediate cases, as the friction coefficient increased the axial pressure measurements moved from the non-frictional case toward the infinite friction one, showing an evident similarity and almost correspondence with the latter when $\phi = 20°$ (namely $\mu = tg20° = 0.360$). Therefore, as the friction increased the axial swelling pressure measurements recorded in the compacted bentonite block and PLs diverged more. Consequently, the recorded top axial swelling pressures differed for tests MGR23 and MGR27. This was due to the fact that those measurements were relative respectively to the CB-layer and to the pellets one, i.e. different final swelling potentials. Measurements recorded in the same material type were however similar with values ranging between the maximum (4 MPa) exerted in the block part of test MGR23 and minimum (1 MPa) exerted in the pellets part of test MGR27 for the sticking case and the value equal to 2 MPa of the non-frictional case.

Fig. 7 presents the comparison between numerical results considering different friction coefficients with the cell wall with respect to the total radial swelling pressure measured at z = 75 mm from the wetting surface (named "top measurements" in the CB-layer for test MGR23 and PL for test MGR27) and at z = 25 mm from the wetting surface (named "bottom measurements" in the PL for test MGR23 and CB-layer for test MGR27) over time. The radial stress analysis at different locations may be of interest because it multiplies the friction coefficient resulting in the maximum resistance to sliding accordingly to the selected failure criteria. In conformity with Eq. (7), frictional stress resulted proportional to radial stress and friction coefficient, hence it manifested its maximum value in the CB layers. On the contrary, material sliding at the bentonite/steel interface resulted the largest as the lowest friction coefficient was set, causing greater CB swelling and PL compaction. Tests MGR23 and MGR27 presented similar features. For all the friction coefficients, an evident radial swelling pressure gradient could be detected, characterised by the maximum value recorded in the CB part (namely on the top for test MGR23 and on the bottom for test MGR27) and very low effect in the pellets one. This result was consistent with Martikainen and Laurila (2018), which measured axial and radial pressures over time in a MX80 bentonite assembly composed of low density pellets and high-density compacted block layers and recorded the higher measurements in the block part. The amplitude of the gradient was proportional to the selected friction coefficient (and consequentially to the frictional stress) being maximum for $\mu = \infty$ and minimum for $\mu = 0$. The maximum radial pressure was recorded in the CB-layer for the sticking case with a value equal to 4 MPa and the minimum one in the PL with 1 MPa for both tests MGR23 and 27.

Indeed, radial pressure measurements corresponding to the CB or PLs for both tests reported similar time evolution and final stabilised values. Also in this case, as the friction coefficient increased, the radial pressure recorded in the CB-layer moved from the non-frictional case toward the sticking contact one for intermediate friction coefficient values. The axial and radial pressure values recorded during test MGR23 for the sticking contact case ($\mu = \infty$) were similar, highlighting an isotropic stress state similar to the one detected in the pellets part for tests MGR23 and MGR27 for all the friction coefficients.

The comparison between experimental and numerical results considering different friction coefficients with the cell wall with respect to the total top axial pressure measured in the CB-layer for test MGR23 and in the pellets one for test MGR27 is given in Fig. 8. The experimental records laid between the non-frictional case pressure evolution and the one concerning $\phi = 10°$ for test MGR23 and for $\phi = 20°$ for test MGR27, not only in terms of values but also with respect to the non-monotonic swelling pressure evolution for transient saturation states. The entire work presented in this paper was performed in the hypothesis that friction between bentonite and cell wall remained constant through all the test duration and for any saturation level. Further studies might be needed in order to asses the truthfulness of the given assumption.

6. Conclusions

The aim of the present research was to examine hydro-mechanical phenomena taking place during the hydration of two-component (initial high density compacted bentonite block and initial low density pellet mixtures): the interaction between them and with the cell stainless steel wall through the development of friction. This purpose was achieved by taking advantage of a combined experimental and numerical

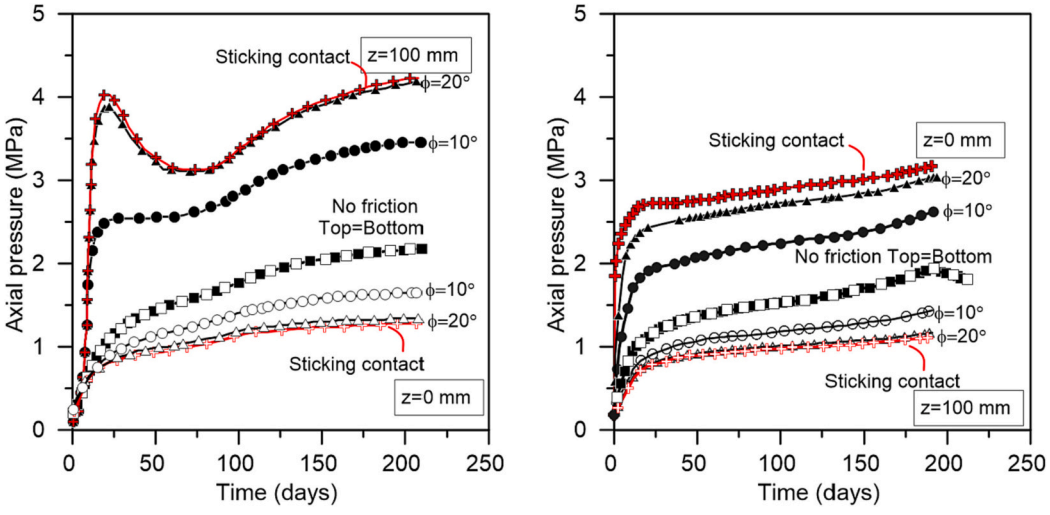

Fig. 6. Total axial top (z = 100 mm) and bottom (z = 0 mm) pressure evolution for tests MGR23 (left) and test MGR27 (right). Comparison between numerical results with different friction coefficients with the cell wall.

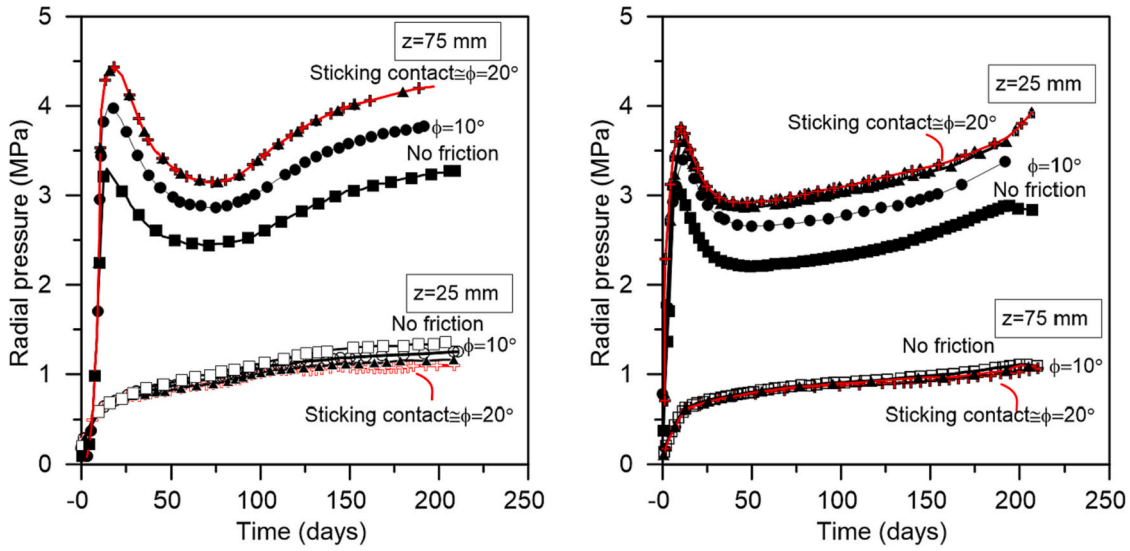

Fig. 7. Radial pressure evolution at $z = 75$ mm from the wetting surface and at $z = 25$ mm from the wetting surface for tests MGR23 (left) and MGR27 (right). Comparison between numerical results with different friction coefficients with the cell wall.

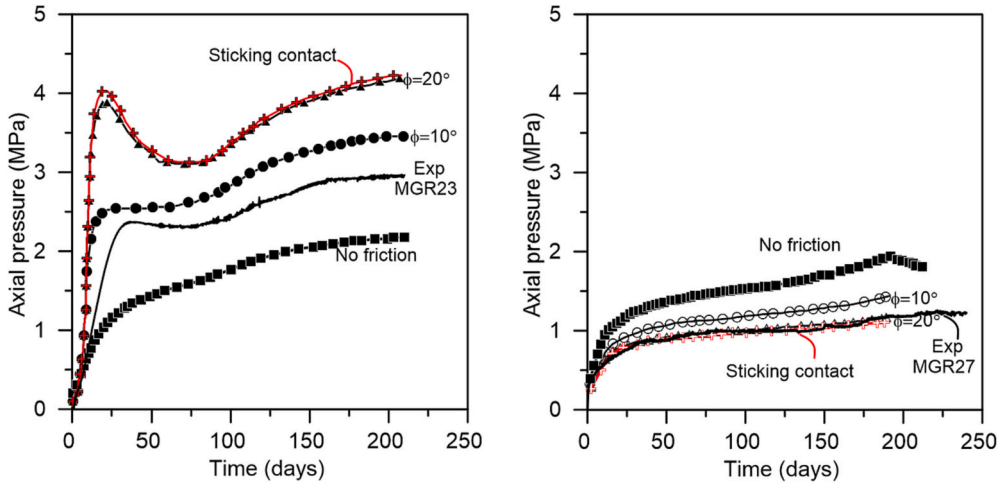

Fig. 8. Top swelling pressure in axial time evolution for test MGR23 (left) and test MGR27 (right). Comparisons between experimental data and model predictions with different friction coefficients with the cell wall.

approach: the five experimental isochoric hydration tests were numerically simulated and coupled hydro-mechanical analyses were conducted with the Barcelona Basic Model and hydraulic double porosity constitutive models.

The experimental campaign (reported in detail in Villar et al., 2021) and the exhaustive numerical study allowed a precise comprehension of the differences in pressure measurements of the laboratory tests by modelling friction between the material samples and the cell wall. The results of this investigation showed that such heterogeneous material combinations affect the distribution and the development of swelling pressure of a given bentonite assembly subjected to hydration, highlighting the role of friction development between the bentonite and the cell wall. This study provided an improved understanding on unexpected experimental data by spotlighting the relevance of frictional phenomena on the pressure measurements results. A sensitivity analysis on the influence of the friction coefficient was performed resulting in the proposition of a range of friction coefficient values.

In addition, the modelled water transfer mechanism (i.e. the permeability) clearly depicted that the combination of pellets and CB-layers plays a major role in the determination of the full-saturation time. In line with this, the dry density and water content evolutions and distributions were affected by the initial heterogeneity configurations. The good agreement between the numerical results and the experimental data, both qualitatively and quantitatively, allowed validating the developed hypothesis and the prediction capability of the model especially concerning the assumption of friction development between the sample and the cell wall during the tests.

In the context of nuclear waste disposals design, these results permitted gaining confidence on barriers safeness, because the improvement provided in terms of predictions of pressure distributions, saturation time and consequently barrier homogeneization shows that a better understanding of barrier performance and behaviour was achieved.

CRediT authorship contribution statement

Liliana Gramegna: Conceptualization, Methodology, Formal analysis, Writing – original draft. **María Victoria Villar:** Investigation, Funding acquisition, Writing – review & editing. **Frédéric Collin:** Writing – review & editing. **Jean Talandier:** Resources, Funding

acquisition. **Robert Charlier:** Conceptualization, Writing – review & editing.

Declaration of Competing Interest

The authors declare that they have no known competing financial interests or personal relationships that could have appeared to influence the work reported in this paper.

Data availability

Data will be made available on request.

References

Abed, A.A., Solowski, W.T., 2019. Simulation of swelling pressure evolution during infiltration in a bentonite block-pellet laboratory scale test. Japan. Geotechn. Soc. Spec. Publ. 7 (2), 323–330.

Alonso, E.E., Gens, A., Josa, A., 1990. A constitutive model for partially saturated soils. Géotechnique 40 (3), 405–430.

Alonso, E.E., Hoffmann, C., Romero, E., 2010. Pellet mixtures in isolation barriers. J. Rock Mech. Geotech. Eng. 2 (1), 12–31. https://doi.org/10.3724/SP.J.1235.2010.00012.

Baryla, P., et al., 2018. Bentonite Mechanical Evolution – Experimental Work for the Support of Model Development and Validation. Technical Report - BEACON Project.

Bernachy-Barbe, F., Conil, N., Guillot, W., Talandier, J., 2020. Observed heterogeneities after hydration of MX-80 bentonite under pellet / powder form. Appl. Clay Sci. 189 https://doi.org/10.1016/j.clay.2020.105542.

Collin, F., Li, X.L., Radu, J.P., Charlier, R., 2002. Thermo-hydro-mechanical coupling in clay barriers. Eng. Geol. 64 (2–3), 179–193.

Cui, Y.J., 2017. On the hydro-mechanical behaviour of MX80 bentonite-based materials. J. Rock Mech. Geotech. Eng. 9 (3), 565–574. https://doi.org/10.1016/j.jrmge.2016.09.003.

Dardé, B., et al., 2018. Hydro-mechanical behaviour of high-density bentonite pellet upon partial hydration. Geotechn. Lett. 8 (4), 1–23.

Dieudonné, A.C., Della Vecchia, G., Charlier, R., 2017. Water retention model for compacted bentonites. Can. Geotech. J. 54 (7), 915–925.

Dueck, A., Nilsson, U., 2010. Tr-10-55 Thermo-Hydro-Mechanical Properties of MX-80. Results from Advanced Laboratory Tests. Technical Report - SKB.

Dueck, A., et al., 2019. Bentonite Homogenisation Laboratory Study, Model Development and Modelling of Homogenisation Processes. www.skb.se.

Gramegna, L., et al., 2020. Hydro-mechanical behaviour of a pellets based bentonite seal: numerical modelling of lab scale experiments. E3S Web Conf. 195, 04009.

Gramegna, L., et al., 2022. Pore size distribution evolution in pellets based bentonite hydration: comparison between experimental and numerical results. Eng. Geol. 304 (May).

Hoffmann, C., Alonso, E.E., Romero, E., 2007. Hydro-Mechanical Behaviour of Bentonite Pellet Mixtures. Phys. Chem. Earth 32, 832–849.

Labalette, T., Harman, A., Dupuis, M.C., Ouzounian, G., 2009. Cigeo, the French geological repository project. In: Waste Management Conference, WM2013, Phoenix, USA, p. 9.

Liu, Z.R., et al., 2019. Particle size ratio and distribution effects on packing behaviour of crushed GMZ bentonite pellets. Powder Technol. 351, 92–101. https://doi.org/10.1016/j.powtec.2019.03.038.

Liu, Z.R., Cui, Y.J., Ye, W.M., Chen, B., et al., 2020a. Investigation of the hydro-mechanical behaviour of GMZ bentonite pellet mixtures. Acta Geotech. 15 (10), 2865–2875. https://doi.org/10.1007/s11440-020-00976-y.

Liu, Z.R., Cui, Y.J., Ye, W.M., Zhang, Z., et al., 2020b. Investigation on vibration induced segregation behaviour of crushed GMZ bentonite pellet mixtures. Constr. Build. Mater. 241, 117949. https://www.sciencedirect.com/science/article/pii/S0950061819334026.

Lloret, A., et al., 2003. Mechanical behaviour of heavily compacted bentonite under high suction changes. Géotechnique 53 (1), 27–40. https://doi.org/10.1680/geot.2003.53.1.27.

Martikainen, J., Laurila, T., 2018. Laboratory tests to evaluate bentonite homogenization. Saanio & Riekkola Oy, Helsinki.

Molinero, A., et al., 2017. In-depth characterisation of a mixture composed of powder / pellets MX80 bentonite. Appl. Clay Sci. 135, 538–546.

Molinero, A., et al., 2018. Investigation of the hydro-mechanical behaviour of a pellet/powder MX80 bentonite mixture using an infiltration column. Eng. Geol. 243 (June), 18–25. https://doi.org/10.1016/j.enggeo.2018.06.006.

Navarro, V., et al., 2020. From double to triple porosity modelling of bentonite pellet mixtures. Eng. Geol. 274 (June), 105714 https://doi.org/10.1016/j.enggeo.2020.105714.

Pusch, R., 1979. Highly compacted sodium bentonite for isolating rock-deposited radioactive waste products. Nucl. Technol. 45, 153–157.

Romero, E., 2013. A microstructural insight into compacted clayey soils and their hydraulic properties. Eng. Geol. 165, 3–19.

Romero, E., Della Vecchia, G., Jommi, C., 2011. An insight into the water retention properties of compacted clayey soils. Géotechnique 61 (4), 313–328. https://doi.org/10.1680/geot.2011.61.4.313.

Salo, J.-P., Kukkola, T., 1989. Bentonite Pellets, an Alternative Buffer Material for Spent fuel Canister Deposition Holes. In: Workshop "Sealing of Radioactive Waster Repositories". Braunschweig.

Sellin, P., Leupin, O.X., 2014. The use of clay as an engineered barrier in radioactive-waste management - a review. Clay Clay Miner. 61 (6), 477–498.

Stavropoulou, E., 2017. Comportement Différé Des Interfaces Argilite/Béton: Caractérisation et Modélisation. Universite' Grenoble-Alpes.

Talandier, J., 2018. Specifications for BEACON WP5: Testing, Verification and Validation of Models Step 1- Verification Cases. Technical Report - BEACON Project.

Van Geet, M., Volckaert, G., Roels, S., 2005. The use of microfocus X-Ray computed tomography in characterising the hydration of a clay pellet/powder mixture. Appl. Clay Sci. 29 (2), 73–87.

Villar, M.V., Iglesias, R.J., Gutiérrez-Álvarez, C., Carbonell, B., 2021. Pellets/block bentonite barriers: laboratory study of their evolution upon hydration. Eng. Geol. 292.

Wang, Q., et al., 2013. Hydraulic conductivity and microstructure changes of compacted bentonite / sand mixture during hydration. Eng. Geol. 164, 67–76. https://doi.org/10.1016/j.enggeo.2013.06.013.

Zhang, Z., et al., 2020. Mechanical behavior of GMZ bentonite pellet mixtures over a wide suction range. Eng. Geol. 264, 325–336. https://doi.org/10.1016/j.clay.2015.10.015.